

CrossMark
click for updatesCite this: *RSC Adv.*, 2015, 5, 93623

Atomistic approach to design favored compositions for the ternary Al–Mg–Ca metallic glass formation

S. Zhao, J. H. Li,* J. B. Liu, S. N. Li and B. X. Liu

An interatomic potential is first constructed for the Al–Mg–Ca system under the formalism of long-range smoothed second-moment approximation of tight-binding scheme, and then applied in Monte Carlo simulations to compare the relative stability of a crystalline solid solution *versus* its disordered counterpart using solid solution models. Simulation results not only predict a glass formation region (GFR), within which the Al–Mg–Ca metallic glass formation is energetically favoured, but also derive the amorphisation driving force (ADF), *i.e.*, the energy difference between the solid solution and disordered state. The ADF is proposed to be positively correlated to the glass forming ability (GFA), suggesting that the larger the ADF is, the easier it is to produce the amorphous alloy and the more stable it is. Moreover, Voronoi tessellation analysis shows a distinct arrangement of Al (Mg, Ca)-centered cluster, correlating closely to the atomic radii and the formation energy of the components. The predictions are fairly consistent with the experimental results reported so far.

Received 3rd July 2015
Accepted 26th October 2015

DOI: 10.1039/c5ra12956g

www.rsc.org/advances

1. Introduction

By exhibiting excellent properties, such as high yield strength, hardness, elastic strain limit, and corrosion resistance,^{1–3} bulk metallic glasses (BMGs) are expected to be promising materials for various applications and have attracted wide interest since their discovery.^{4–6} To date, BMGs have been obtained in many binary, ternary and multi-component metal systems. However, some basic issues, for instance, the glass formation and atomic configuration, have not been satisfactorily clarified yet. To predict the glass formation, Turnbull⁷ proposed a deep eutectic criterion based on the equilibrium phase diagram. Egami and Waseda⁸ have also proposed the atomic size difference rule based on atomic level stresses. Liu⁹ *et al.* have proposed a structural difference rule, predicting that amorphous alloys would most likely be formed in a system containing different crystalline structured metals. Thermodynamic calculations^{10,11} have also been applied to predict the metallic glass formation. In the authors' view, there is an alternative way to predict the glass formation compositions using interatomic potential. If a realistic interatomic potential of a metallic system is constructed and the interactions between the atoms are known, then the glass formation compositions, as well as other physical properties, can be determined through relevant simulations.^{9,12}

Recently, Al-based and Ca–Mg-based bulk metallic glasses have become popular alloys in this field.^{13–26} It is found that cylinder-shaped amorphous rods with diameters up to 1 mm

are produced for the binary Al–Ca alloys with 33–35 at% Al. The introduction of Mg has extended the as-cast amorphous rod size to 2 mm in diameter.²⁷ Therefore, we selected the promising Al–Mg–Ca ternary alloy as the model system. In this study, the glass formation and atomic level structure of the Al–Mg–Ca ternary metallic glasses are investigated using a newly constructed Al–Mg–Ca interatomic potential as a starting base before conducting relevant Monte Carlo simulations.

2. Construction of Al–Mg–Ca interatomic potential

The interatomic potential was constructed for the Al–Mg–Ca system under the framework of a long-range smoothed second-moment-approximation of tight-binding (TB-SMA) scheme:^{28,29}

$$E_i = \frac{1}{2} \sum_{j \neq i} \varphi(r_{ij}) - \sqrt{\sum_{j \neq i} \psi(r_{ij})} \quad (1)$$

where E_i is the potential energy of atom i . The first and second terms in the right side of eqn (1) are pair item and n-body item respectively. The variable r_{ij} is the distance between atoms i and j . The φ and ψ can be expressed as:

$$\varphi(r_{ij}) = \begin{cases} 2A_1 \exp \left[-p_1 \left(\frac{r_{ij}}{r_0} - 1 \right) \right], & r_{ij} \leq r_{m1} \\ 2A_{1m} \exp \left[-p_{1m} \left(\frac{r_{ij}}{r_0} - 1 \right) \right] \left(\frac{r_{c1}}{r_0} - \frac{r_{ij}}{r_0} \right)^{n_1}, & r_{m1} < r_{ij} \leq r_{c1} \end{cases} \quad (2)$$

Key Laboratory of Advanced Materials (MOE), School of Materials Science and Engineering, Tsinghua University, Beijing 100084, China. E-mail: lijiahao@mail.tsinghua.edu.cn

Table 1 The fitted potential parameters of Al–Mg–Ca system

	Al	Mg	Ca	Al–Mg	Al–Ca	Mg–Ca
p_1	8.776460	10.37307	9.780032	10.23828	5.508843	9.118697
A_1 (eV)	0.402184	0.145780	0.165598	0.190712	0.818938	0.246665
r_{m1} (Å)	2.764394	3.522308	3.715213	2.654430	3.041843	2.967012
n_1	4	4	4	4	4	4
p_{1m}	2.588558	3.850843	3.413309	3.447698	1.667659	4.019030
A_{1m} (eV)	2.917212	0.538535	1.446073	3.457160	0.777224	1.442271
r_{c1} (Å)	4.607023	5.487015	6.167967	4.421070	6.302642	5.723657
p_2	5.249466	4.375061	4.814647	3.439821	5.062842	4.380322
A_2 (eV ²)	4.738155	0.951887	1.232266	1.890899	7.267646	1.490516
r_{m2} (Å)	3.786874	2.588516	3.908279	2.636021	4.52141	3.008100
n_2	5	5	5	5	5	5
p_{2m}	0.000477	0.000378	0.000389	0.000438	0.000386	0.000389
A_{2m} (eV ²)	1.114067	1.130393	1.014402	0.441637	0.817211	1.445114
r_{c2} (Å)	6.515324	6.250000	7.962903	6.996059	7.614118	7.020142
r_0 (Å)	2.864321	3.203567	3.904000	2.999131	3.131331	3.514492

Table 2 Lattice constants (a and c), cohesive energies E_c , elastic constants C_{ij} and bulk moduli B_0 of Al, Mg and Ca fitted using the potential and obtained from experimental dates or *ab initio* calculations

	Fcc-Al (ref. 31)		Hcp-Mg (ref. 19)		Fcc-Ca	
	Fitted	Exp	Fitted	Exp	Fitted	<i>ab</i>
a (Å)	4.051	4.050	3.209	3.209	5.521	5.521
c (Å)			5.235	5.211		
E_c (eV)	3.387	3.390	1.508	1.510	1.839	1.840
C_{11} (Mbar)	0.821	1.067	0.591	0.595	0.219	0.186
C_{12} (Mbar)	0.705	0.605	0.270	0.261	0.149	0.157
C_{13} (Mbar)			0.223	0.218		
C_{33} (Mbar)			0.642	0.616		
C_{44} (Mbar)	0.289	0.283	0.112	0.164	0.143	0.088
B_0 (Mbar)	0.743	0.722	0.362	0.354	0.168	0.167

$$\psi(r_{ij}) = \begin{cases} A_2 \exp \left[-p_2 \left(\frac{r_{ij}}{r_0} - 1 \right) \right], & r_{ij} \leq r_{m2} \\ A_{2m} \exp \left[-p_{2m} \left(\frac{r_{ij}}{r_0} - 1 \right) \right] \left(\frac{r_{c2}}{r_0} - \frac{r_{ij}}{r_0} \right)^{n_2}, & r_{m2} < r_{ij} \leq r_{c2} \end{cases} \quad (3)$$

where P_1 , A_1 , r_{m1} , A_{1m} , r_{c1} , P_{1m} , P_2 , A_2 , r_{m2} , A_{2m} , r_{c2} and P_{2m} are the potential parameters to be fitted, whereas n_1 and n_2 are 4 and 5, respectively. Readers can refer to the ref. 28 for more details on the potential parameters.

The potential parameters of Al–Al, Mg–Mg and Ca–Ca were determined by fitting to the lattice constants, cohesive energies, elastic constants and bulk moduli of the Al, Mg and Ca metals. The parameters of the cross potentials Al–Mg, Al–Ca and Mg–Ca were determined by fitting to the lattice constants, formation energies and bulk moduli of their stable or metastable compounds in these systems, such as *c*58–Al₁₂Mg₁₇, *a*P22–Al₃Ca₈ and *h*R12–Mg₂Ca. Because of lacking adequate experimental data for the related compounds, *ab initio* calculations were conducted to derive the relevant physical properties of the compounds using the Cambridge Serial Total Energy Package (CASTEP)³⁰ to assist in constructing the interatomic n-body potential. The fitted potential parameters of the Al–Mg–Ca system are listed in Table 1. It is noted that the potential parameters of Al and Mg was adopted from our previous works.^{19,31} Tables 2 and 3 give the cohesion energies, elastic constants and bulk moduli, which are reproduced from potential or obtained in experiments or *ab initio* calculations.^{32–34} It can be seen that the physical properties obtained from potential match well with the experimental results or *ab initio* calculations.

To evaluate the validity of the fitted potential, the equation of state (EOS) is derived from the potential and compared with the Rose equation.³⁵ The pair terms, n-body parts and the total energies reproduced from the interatomic potential, together with the corresponding Rose equations, are all shown in Fig. 1 and 2. The EOSs derived from the proposed potential agree well

Table 3 The properties reproduced from interatomic potential (first line) and calculated *via ab initio* methods (second line) of Al–Mg, Al–Ca and Mg–Ca compounds

Compounds	Al ₃ Mg	AlMg	Al ₁₂ Mg ₁₇	Al ₃ Ca	AlCa	Al ₃ Ca ₈	MgCa ₂	MgCa	Mg ₂ Ca
Space group	<i>Pm3m</i>	<i>Pm3m</i>	<i>I43m</i>	<i>Pm3m</i>	<i>Pm3m</i>	<i>P1</i>	<i>I4/mmm</i>	<i>Pm3m</i>	<i>P6₃/mmc</i>
a or a , c or a , b , c (Å)	4.1682	3.4237	10.5914	4.2858	3.6908	9.4782, 9.4214, 9.9190	4.033, 13.785	4.099	6.334, 10.310
	4.1560	3.4018	10.5679	4.3077	3.7143	9.4616, 9.5349, 9.6197	3.943, 13.547	3.970	6.245, 10.112
E_c (eV)	2.913	2.379	2.305	3.155	2.816	2.426	1.790	1.766	1.746
	2.913	2.378	2.305	3.156	2.813	2.428	1.789	1.768	1.746
B_0 (Mbar)	0.6364	0.4902	0.4875	0.5276	0.2984	0.2488	0.2373	0.2614	0.3095
	0.6390	0.4717	0.4912	0.5608	0.3684	0.2424	0.2174	0.2484	0.2854

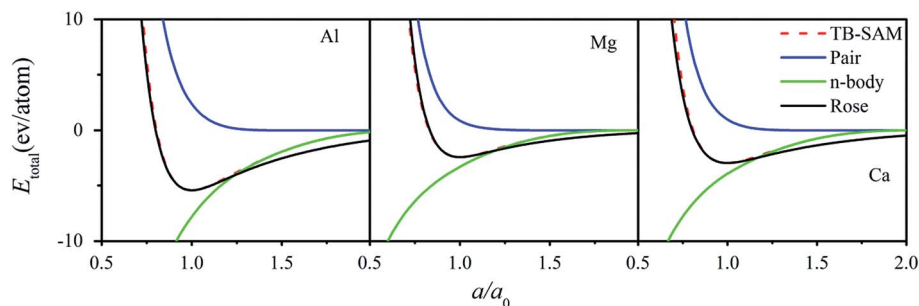


Fig. 1 Total energies, pair terms and n-body parts as a function of lattice constant calculated from the interatomic potential and Rose equation for Al, Mg and Ca.

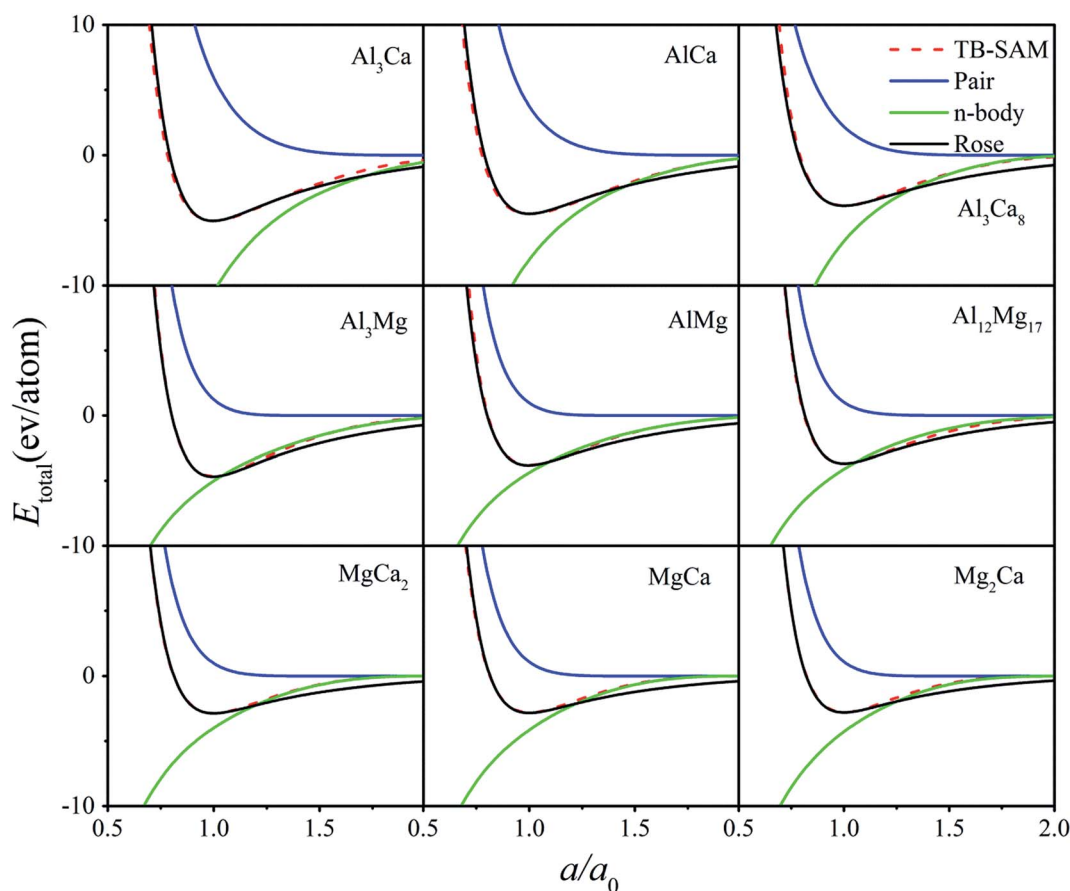


Fig. 2 Total energies, pair terms and n-body parts as a function of lattice constant calculated from the interatomic potential and Rose equation for compounds of AlCa, AlMg, MgCa, Al₃Mg, Al₃Ca, MgCa₂, Mg₂Ca, Al₃Ca₈, Al₁₂Mg₁₇.

with the corresponding Rose equations, indicating that the constructed Al-Mg-Ca potential could be applied to describe the atomic interactions of the system even far from the equilibrium state. It can be seen that the pair terms, n-body parts and the total energy of these structures are smooth and continuous over the entire range without any 'jumps' or discontinuities. In other words, the potential energy and its derivatives expressed by eqn (2) and (3) go to zero continuously and smoothly at the cutoff distance, thus removing the leaps of energy and force and avoiding some non-physical behaviours in

the simulation.³⁶ This suggests that the newly constructed potentials under the formalism of TB-SMA are adequate for describing the interatomic interactions in the Al-Mg-Ca system.

3. Simulation models and characterisation methods

The formation of metallic glasses is always a non-equilibrium process. Due to severe limitation of kinetic conditions,

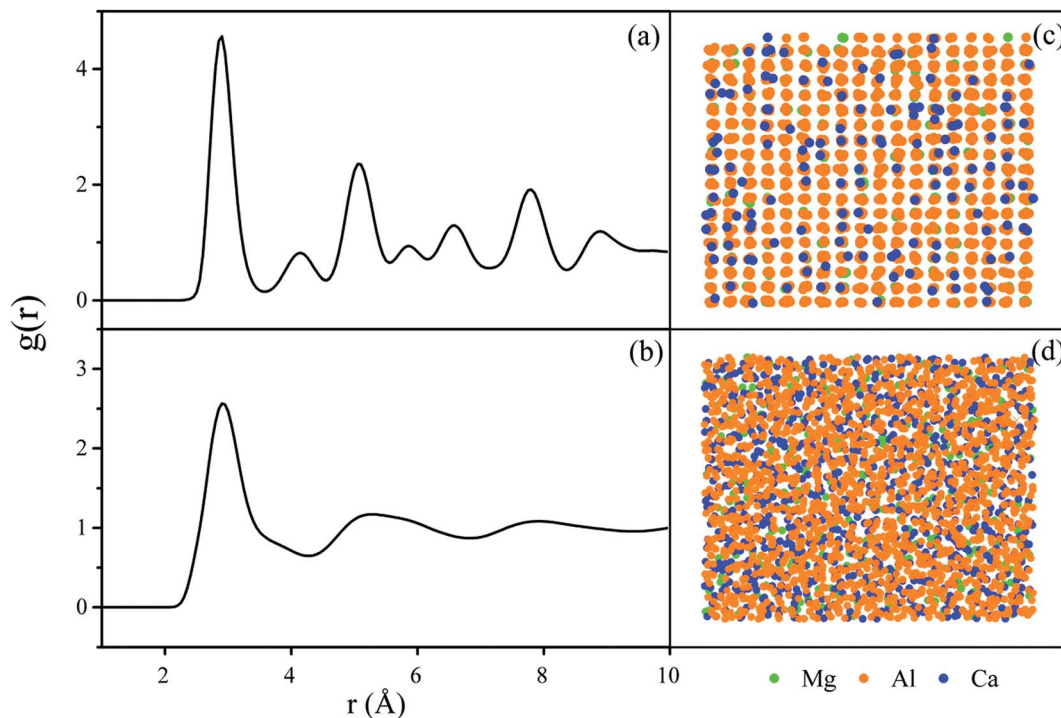


Fig. 3 The total pair-correlation functions $g(r)$, atomic position projections of the crystalline state $\text{Al}_{85}\text{Mg}_{10}\text{Ca}_5$ (a and c) and the amorphous state $\text{Al}_{60}\text{Mg}_{10}\text{Ca}_{30}$ (b and d). Orange circles are for Al, green circles are for Mg and blue circles are for Ca.

complicated intermetallic compounds are not able to nucleate and grow. Therefore, the phase competing against the metallic glass is frequently the solid solution of a simple structure. Consequently, the issue related to glass formation is converted into comparing the relative stability of the solid solution to its amorphous counterpart.^{9,37–39} Based on the Al–Mg–Ca potential, Monte Carlo simulations were performed in this work to study the relative stability of the solid solution and amorphous phases.

Because the stable crystalline structures of Al, Mg and Ca are fcc, hcp and fcc, respectively, two types of solid solution models, *i.e.*, the fcc and hcp solid solution models, were constructed based on which type of atoms are dominant in the alloy composition. For fcc models, the [100], [010] and [001] crystalline directions are parallel to the x , y and z axes, respectively, while for the hcp model, the [100], [001] and [120] crystalline directions are parallel to the x , y and z axes, respectively. Periodic boundary conditions were applied in the three directions. The fcc and hcp solid solution models consist of 2916 ($9 \times 9 \times 9 \times 4$) atoms and 2912 ($13 \times 8 \times 7 \times 4$) atoms, respectively. In constructing the solid solution models, the solvent atoms were substituted randomly by a certain number of solute atoms to obtain a desired composition. The initial solid solutions were annealed at zero pressure and 300 K under isothermal–isobaric ensemble to permit sufficient simulation time to reach a relatively stable state in which the related dynamic variables exhibited no secular variations. The structures of the alloys obtained in the MC simulation were then collected and analyzed using total pair-correlation functions $g(r)$ and the method of Voronoi tessellation.

3.1 Glass formation region of the Al–Mg–Ca system

Based on the solid solution models, MC simulations were carried out over the entire composition triangle of the system. For a solid solution of $\text{Al}_x\text{Mg}_y\text{Ca}_{1-x-y}$, the values of x and y varied over a composition interval of 5% to cover the range from 0 to 100%. The initial lattice parameter of each solid solution was determined according to Vegard's law.

After adequate MC simulation time, the initially solid solution models reached a relatively stable state, and it is found that the models exhibited two different states with varying compositions, *i.e.*, either retaining the initial crystalline state or collapsing into a disordered state. Taking the $\text{Al}_{60}\text{Mg}_{10}\text{Ca}_{30}$ and $\text{Al}_{85}\text{Mg}_{10}\text{Ca}_5$ models as examples, Fig. 3 shows the total pair-correlation functions $g(r)$ and atomic position projections of these two models. From Fig. 3(a), it is obvious that the $g(r)$ curve of $\text{Al}_{85}\text{Mg}_{10}\text{Ca}_5$ shows crystalline peaks, suggesting a long-range ordered state, and the atomic position projection in Fig. 3(c) also shows a regular array. For $\text{Al}_{60}\text{Mg}_{10}\text{Ca}_{30}$, as seen in Fig. 3(b), all the peaks beyond the second disappeared, exhibiting a typical short-range ordered and long range disordered feature. This is also supported by Fig. 3(d), indicating that the crystalline lattice has collapsed into a completely amorphous state.

Simulations over the entire Al–Mg–Ca composition triangle allow us to construct a diagram of glass formation, according to $g(r)$ and atomic position projections of each specific alloy, as shown in Fig. 4. The composition triangle was divided into three regions by two critical solubility lines, *i.e.*, the fold-line ABC and the straight line DE. When an alloy composition is located beyond the lines and moves toward the Ca corner, or beyond

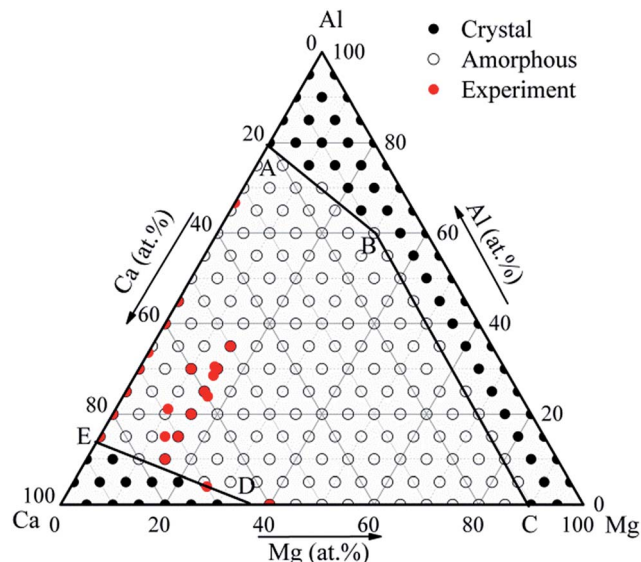


Fig. 4 The glass forming stoichiometry diagram derived from the MC simulations at 300 K for the Al–Mg–Ca ternary system.

line ABC and moves toward the Al–Mg side, the crystalline structure could keep stable. These regions are consequently classified as the crystalline regions. When the composition falls into the central pentagonal region, enclosed by ABCDE, the crystalline structure would become unstable and spontaneously collapses into an amorphous state. This pentagonal region is therefore defined as the glass formation region (GFR). Experimental observations reported so far in the literature have been extensively collected^{14,17,27,40,41} and marked in Fig. 4 by red dots. It is seen that these experimentally measured glass formation compositions mostly fall within the predicted pentagon region, suggesting that the results predicted by MC simulations for the Al–Mg–Ca system are quite reasonable.

3.2 Composition optimization for glass formation

To design the composition of Al–Mg–Ca metallic glasses, it is necessary to search for the best composition, *i.e.*, the largest glass-forming ability. It has been argued that the amorphisation driving force (ADF), *i.e.*, the energy difference between the solid solution and disordered state is correlated positively with the glass forming ability (GFA), suggesting that the larger the ADF is, the easier it is to produce or the more stable the amorphous alloy is. Consequently, the energy differences, $\Delta E^{\text{am-s.s}}$, of the $\text{Al}_x\text{Mg}_y\text{Ca}_{1-x-y}$ solid solutions and its disordered counterpart were calculated and defined as the driving forces for crystalline-to-amorphous transition. The $\Delta E^{\text{am-s.s}}$ can be written as:

$$\Delta E^{\text{am-s.s}} = \Delta E^{\text{am}} - \Delta E^{\text{s.s}} \quad (4)$$

where ΔE^{am} is the formation energy of the amorphous phase and $\Delta E^{\text{s.s}}$ is the formation energy of the solid solutions. The optimised glass forming composition could be determined by searching for the minimum $\Delta E^{\text{am-s.s}}$ in the glass-formation region. Assume that E_{am} is the energy per atom of the Al–Mg–

Ca amorphous phase and E_{Al} , E_{Mg} and E_{Ca} are the lattice energies of Al, Mg, Ca respectively. Thus the formation energy for the amorphous phase ΔE^{am} can be expressed by:

$$\Delta E^{\text{am}} = E_{\text{am}} - [xE_{\text{Al}} + yE_{\text{Mg}} + (1 - x - y)E_{\text{Ca}}] \quad (5)$$

To determine $\Delta E^{\text{s.s}}$, the relevant MC method is also performed to relax the solid solutions, *i.e.*, reach the lowest energy E_{min} . The ideal solid solution was obtained by annealing the simulation model, optimising its lattice constant and simultaneously keeping the crystal symmetry unchanged. The $\Delta E^{\text{s.s}}$ can then be determined by

$$\Delta E^{\text{s.s}} = E_{\text{min}} - [xE_{\text{Al}} + yE_{\text{Mg}} + (1 - x - y)E_{\text{Ca}}] \quad (6)$$

The driving force for metallic glass formation was thus obtained and shown in Fig. 5. One can see from the figure that the energy difference $\Delta E^{\text{am-s.s}}$ is negative over the entire GFR, suggesting that the energy of the amorphous phase is lower than that of the solid solution, and showing the formation of the amorphous phase is indeed energetically favored. Moreover, the larger the energy difference, the stronger the driving force for glass formation. We define this sub-region around the composition with a minimum $\Delta E^{\text{am-s.s}}$ as the optimized compositions for Al–Mg–Ca metallic glass formation, within which the alloys have a greater GFA than those alloys located outside the sub-region. It follows that the Al–Mg–Ca amorphous alloys with the optimal compositions are expected to be more attainable or more thermally stable than other alloys in the system, thus providing the basic guidelines to design appropriate alloy compositions for producing Al–Mg–Ca metallic glasses.

The diameter of the amorphous rods obtained so far are collected and shown in Fig. 5. One notes that the diameters of $\text{Al}_{30}\text{Mg}_{15}\text{Ca}_{55}$ and $\text{Al}_{28.5}\text{Mg}_{15}\text{Ca}_{56.5}$ glasses are 0.5 and 1.5 mm, $\text{Al}_{29}\text{Mg}_9\text{Ca}_{62}$ and $\text{Al}_{30}\text{Mg}_{10}\text{Ca}_{60}$ are 0.5 and 2 mm respectively.^{17,27} The sizes of metallic glasses are different in different experiments although their compositions are almost the same. It suggests that the glass formation is a very complex process

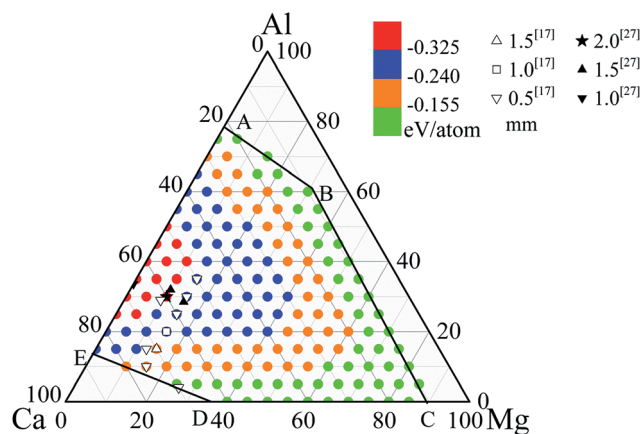


Fig. 5 Amorphous driving forces for the crystalline-to-amorphous transition of the Al–Mg–Ca alloys calculated from MC simulations, and the diameter of some amorphous rods.

and many factors such as, defects and impurity, have effects on the size of obtained metallic glasses. Therefore, the glass-formation abilities measured by the diameters of amorphous rods can be considered as nominal one, and the predicted one by theoretical methods as done in present study, can be considered as intrinsic glass-formation abilities. In general, the nominal GFA would fluctuate around the intrinsic one due to the effects of external factors. Consequently, the proposed correlation between ADF and GFA, *e.g.* the diameter of the amorphous rods, approximately holds. For example, the calculated ADF of $\text{Al}_{10}\text{Mg}_{15}\text{Ca}_{75}$ and $\text{Al}_{30}\text{Mg}_{10}\text{Ca}_{60}$ are -0.1572 and -0.3258 eV per atom, and the corresponding the diameter of the amorphous rods 0.5 and 2 mm, respectively.^{17,27} They indeed show that the larger the ADF of metallic glass and the larger the size of the amorphous rod obtained by experiment. In addition to the complexity of metallic glass formation mentioned above, the performance of constructed potential, the limitation of simulation method and so on could result in the inconsistencies. With further improvement of experiment and simulation, it can be expected that, there will be more observation to confirm the correlation between ADF and the GFA of amorphous alloy. In short, the predicted intrinsic GFR, optimal compositions of the Al–Mg–Ca system as well as the validity of the constructed *n*-body potential are relevant. It also shows the study of crystalline-to-amorphous transition starting from a realistic interatomic potential of a ternary metal system is appropriate.

3.3 Atomic configuration of the $\text{Al}_{10}\text{Mg}_{30}\text{Ca}_{60}$ glasses

In the following, the atomic configurations of $\text{Al}_{10}\text{Mg}_{30}\text{Ca}_{60}$ metallic glasses was analyzed, which is located in the optimal composition sub-region and exhibiting a relatively larger maximum diameter that are found in experiments. Fig. 6 shows the coordination number (CN) of Al, Mg and Ca atoms in the $\text{Al}_{10}\text{Mg}_{30}\text{Ca}_{60}$ metallic glasses. It can be seen that CNs are well-distributed over a wide range, with the most common

coordination numbers being CN = 9 and 10 for Al-centered clusters, CN = 11 and 12 for Mg-centered clusters and CN = 12 and 13 for the Ca-centered clusters. The observed correlation can be understood in terms of the atomic size difference. The Goldschmidt atomic radii of Al, Mg, and Ca are 1.43, 1.60, and 1.97 Å, respectively.³³ The relatively larger atomic size of Ca permits more atoms in the nearest-neighbouring shells and leads to a larger CN, followed by Mg, and then Al. The dense clustering of small-sized and large-sized clusters would lead to an efficient packing in space and the enhancement of the stability.¹⁹

Voronoi tessellation^{42–44} was also carried out to investigate the atomistic configuration of the Al–Mg–Ca metallic glasses. It should be noted that the faces smaller than 5% of the average face area were neglected in counting the CN.^{45,46} The Voronoi index $\langle n_3, n_4, n_5, n_6 \rangle$, where n_i denotes the number of *i*-edged faces in the Voronoi polyhedron,^{42,47,48} is used to characterise the atomic cluster surrounding an atom. Fig. 7 illustrates the types and fractions of Al (Mg, Ca)-centered coordination cluster most frequently found in the amorphous structure. The predominant polyhedron are $\langle 0,4,4,2 \rangle$ and $\langle 1,3,3,2 \rangle$ for Al, $\langle 0,2,8,1 \rangle$ and $\langle 0,3,6,3 \rangle$ for Mg and $\langle 0,3,6,4 \rangle$ and $\langle 0,2,8,4 \rangle$ for Ca. Because the polyhedra of $\langle 0,4,4,2 \rangle$, $\langle 0,2,8,1 \rangle$, $\langle 0,3,6,3 \rangle$, $\langle 0,3,6,4 \rangle$ and $\langle 0,2,8,4 \rangle$ can be considered as icosahedral-like (distorted or irregular icosahedra),^{47,49} the major local structural feature within the optimal composition sub-region exhibits icosahedral-like ordering, which plays an important role to in stabilising the structure of metal–metal amorphous alloys.⁵⁰ Also, Wu *et al.*⁵¹ analysed the cluster energies for different types of local clusters and found that the $\langle 0,2,8,1 \rangle$, $\langle 0,3,6,3 \rangle$, $\langle 0,3,6,4 \rangle$ and $\langle 0,2,8,4 \rangle$ clusters have relative lower energies in metallic glasses. For the system of CaMgZn ,⁴⁸ the similar Voronoi cluster within the better GFA composition range was also found. In most cases, these clusters permit more Ca atoms, while in the Ca-centered cluster, there are slightly more Al atoms than Mg and Al (Mg) is less dominant in the Mg (Al)-centered cluster. The

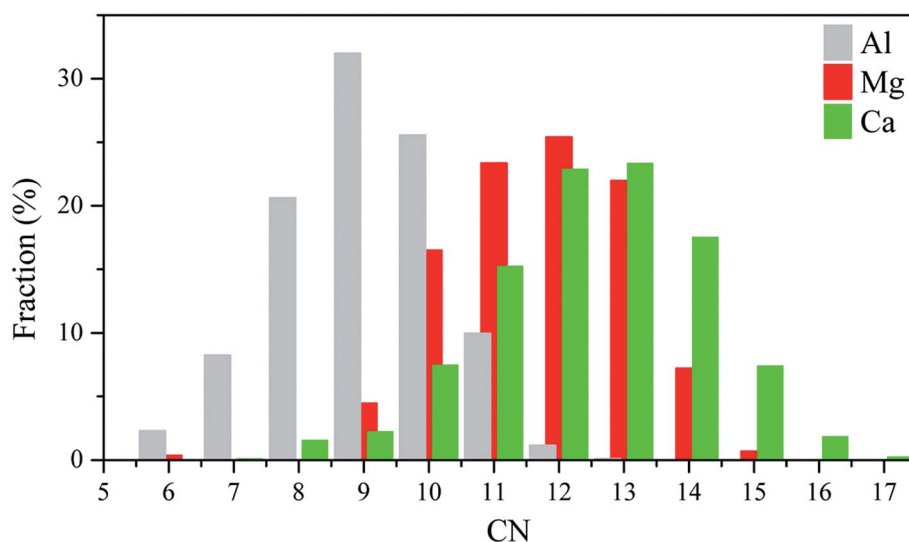


Fig. 6 Spectrum coordination numbers (CNs) for the optimised $\text{Al}_{30}\text{Mg}_{10}\text{Ca}_{60}$ amorphous alloys.

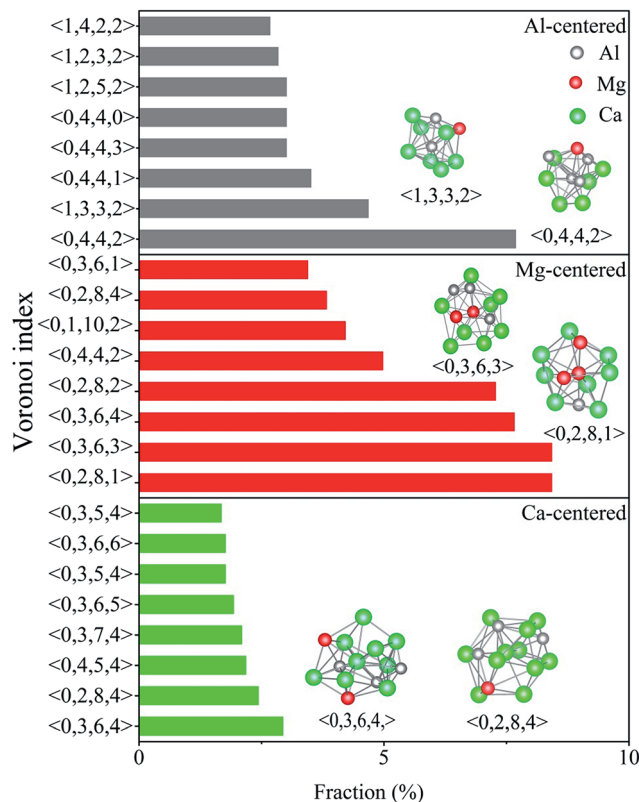


Fig. 7 Types of Al (Mg, Ca)-centered clusters and their fractions in $\text{Al}_{30}\text{Mg}_{10}\text{Ca}_{60}$ amorphous alloys and the topologies of dominant Al (Mg, Ca)-centered clusters with different Voronoi index, $\langle 0,4,4,2 \rangle$ and $\langle 1,3,3,2 \rangle$ for Al, $\langle 0,2,8,1 \rangle$ and $\langle 0,3,6,3 \rangle$ for Mg, $\langle 0,3,6,4 \rangle$ and $\langle 0,2,8,4 \rangle$ for Ca respectively.

arrangement relates to the formation energies which are -20 , -6 and -2 kJ mol^{-1} for Al–Ca, Mg–Ca and Al–Mg, respectively,⁵² resulting in that Ca prefers Al than Mg as nearest-neighbors and the bonds of Al–Mg are less. Thus, the atomic level configurations reduce the total energy of system and lead to a stable state.

4. Conclusion

A realistic interatomic potential was first constructed for the Al–Mg–Ca system under the formalism of TB-SMA and then applied to Monte Carlo simulations. The simulations not only revealed the underlying physics of metallic glass formation is the spontaneous collapse of the crystalline lattice when the solute concentration exceeds a critical value, but also predict an intrinsic glass formation region of the Al–Mg–Ca system. The energy difference between the solid solution and disordered state, *i.e.*, the amorphous driving force (ADF) and is proposed to be positively correlated with the glass forming ability (GFA). The larger the ADF is, the easier the amorphous alloy is to be produced or the more stable the amorphous alloy is. Moreover, an optimal composition sub-region, within which the driving force is larger than the other composition was located, indicating that these alloys are most stable or ready to be produced. Furthermore, Voronoi analysis was performed for the alloy in

the optimised composition sub-region. It is revealed that the local atomic configurations are correlated closely with the atomic size and formation energy of the constituent metals.

Acknowledgements

The authors are grateful for the financial support from the National Natural Science Foundation of China (51131003, 51571129), the Ministry of Science and Technology of China (973 Program 2012CB825700), and the Administration of Tsinghua University.

References

- 1 T. Lin, C. Yong-Qiang, S. Zhi-Wei, L. Ju, W. Cheng-Cai, H. Xiao-Dong, S. Jun and M. Evan, *Nat. Commun.*, 2012, **3**, 609.
- 2 J. Schroers, *Adv. Mater.*, 2010, **22**, 1566–1597.
- 3 W. H. Wang, C. Dong and C. H. Shek, *Mater. Sci. Eng., R*, 2004, **44**, 45–89.
- 4 J. J. Gilman, *J. Appl. Phys.*, 1975, **46**, 1435–1436.
- 5 W. Klement, R. H. Willens and P. Duwez, *Nature*, 1960, **187**, 869–870.
- 6 A. L. Greer and M. F. Ashby, *Scr. Mater.*, 2006, **54**, 321–326.
- 7 D. Turnbull, *Trans. Metall. Soc. AIME*, 1961, **221**, 422–439.
- 8 T. Egami and Y. Waseda, *J. Non-Cryst. Solids*, 1984, **64**, 113–134.
- 9 J. H. Li, X. D. Dai, S. H. Liang, K. P. Tai, Y. Kong and B. X. Liu, *Phys. Rep.*, 2008, **455**, 1–134.
- 10 F. R. de Boer, R. Boom, W. C. M. Mattens, A. R. Miedema and A. K. Niessen, *Cohesion in metals: transition metal alloys*, 1988.
- 11 J. A. Alonso, L. J. Gallego and J. A. Somoza, *Il Nuovo Cimento*, 1990, **12**, 587–595.
- 12 S. H. Liang, Y. Dai, J. H. Li and B. X. Liu, *J. Phys. Chem. B*, 2010, **114**, 9540–9545.
- 13 O. N. Senkov, D. B. Miracle and J. M. Scott, *Intermetallics*, 2006, **14**, 1055–1060.
- 14 O. N. Senkov and J. M. Scott, *Scr. Mater.*, 2004, **50**, 449–452.
- 15 O. N. Senkov and J. M. Scott, *J. Non-Cryst. Solids*, 2005, **351**, 3087–3094.
- 16 O. N. Senkov, J. M. Scott and D. B. Miracle, *J. Alloys Compd.*, 2006, **424**, 394–399.
- 17 O. N. Senkov, J. M. Scott and D. B. Miracle, *Mater. Trans.*, 2007, **48**, 1610–1616.
- 18 K. Ahn, D. Louca, S. J. Poon and G. J. Shiflet, *Phys. Rev. B: Condens. Matter Mater. Phys.*, 2004, **70**, 224103.
- 19 Q. Wang, J. H. Li, J. B. Liu and B. X. Liu, *J. Phys. Chem. B*, 2014, **118**, 4442–4449.
- 20 A. Inoue, K. Ohtera, K. Kita and T. Masumoto, *Jpn. J. Appl. Phys., Part 2*, 1988, **27**, L1796–L1799.
- 21 K. Amiya and A. Inoue, *Mater. Trans.*, 2002, **43**, 81–84.
- 22 K. Amiya and A. Inoue, *Mater. Trans.*, 2002, **43**, 2578–2581.
- 23 X. Gu, G. J. Shiflet, F. Q. Guo and S. J. Poon, *J. Mater. Res.*, 2005, **20**, 1935–1938.
- 24 V. Keppens, Z. Zhang, O. N. Senkov and D. B. Miracle, *Philos. Mag.*, 2007, **87**, 503–508.
- 25 B. Zberg, P. J. Uggowitzer and J. F. Löffler, *Nat. Mater.*, 2009, **8**, 887–891.

- 26 S. N. Li, J. B. Liu, J. H. Li, J. Wang and B. X. Liu, *J. Phys. Chem. B*, 2015, **119**, 3608–3618.
- 27 F. Q. Guo, S. J. Poon and G. J. Shiflet, *Appl. Phys. Lett.*, 2004, **84**, 37–39.
- 28 J. H. Li, X. D. Dai, T. L. Wang and B. X. Liu, *J. Phys.: Condens. Matter*, 2007, **19**, 086228.
- 29 V. Rosato, M. Guillope and B. Legrand, *Philos. Mag. A*, 1989, **59**, 321–336.
- 30 M. D. Segall, P. J. D. Lindan, M. J. Probert, C. J. Pickard, P. J. Hasnip, S. J. Clark and M. C. Payne, *J. Phys.: Condens. Matter*, 2002, **14**, 2717–2744.
- 31 Y. Y. Cui, T. L. Wang, J. H. Li, Y. Dai and B. X. Liu, *Phys. Chem. Chem. Phys.*, 2011, **13**, 4103–4108.
- 32 D. R. Lide and T. J. Bruno, *CRC Handbook of Chemistry and Physics*, CRC Press, New York, 2002.
- 33 C. Kittel, *Introduction to solid state physics*, Wiley, New York, 2002.
- 34 S. L. Shang, A. Saengdeejing, Z. G. Mei, D. E. Kim, H. Zhang, S. Ganeshan, Y. Wang and Z. K. Liu, *Comput. Mater. Sci.*, 2010, **48**, 813–826.
- 35 J. H. Rose, J. R. Smith, F. Guinea and J. Ferrante, *Phys. Rev. B: Condens. Matter Mater. Phys.*, 1984, **29**, 2963–2969.
- 36 D. Frenkel and B. Smit, *Understanding Molecular Simulation: from Algorithms to Applications*, Academic, New York, 2002.
- 37 B. X. Liu, W. S. Lai and Q. Zhang, *Mater. Sci. Eng., R*, 2000, **29**, 1–48.
- 38 J. M. Lopez, J. A. Alonso and L. J. Gallego, *Phys. Rev. B: Condens. Matter Mater. Phys.*, 1987, **36**, 3716–3722.
- 39 H. W. Sheng, G. Wilde and E. Ma, *Acta Mater.*, 2002, **50**, 475–488.
- 40 W. A. Hines, P. Miller, A. Paoluzi, C. L. Tsai and B. C. Giessen, *J. Appl. Phys.*, 1982, **53**, 7789–7791.
- 41 J. Hafner and S. S. Jaswal, *Phys. Rev. B: Condens. Matter Mater. Phys.*, 1988, **38**, 7320–7332.
- 42 H. W. Sheng, W. K. Luo, F. M. Alamgir, J. M. Bai and E. Ma, *Nature*, 2006, **439**, 419–425.
- 43 S. Mechler, G. Schumacher, V. Koteski, H. Riesemeier, F. Schaefer and H. E. Mahnke, *Appl. Phys. Lett.*, 2010, **97**, 041914.
- 44 K. Yashiro, M. Nishimura and Y. Tomita, *Modell. Simul. Mater. Sci. Eng.*, 2006, **14**, 597–605.
- 45 Y. Q. Cheng, E. Ma and H. W. Sheng, *Phys. Rev. Lett.*, 2009, **102**, 245501.
- 46 J. H. Li, S. Z. Zhao, Y. Dai, Y. Y. Cui and B. X. Liu, *J. Appl. Phys.*, 2011, **109**, 113538.
- 47 S. Y. Wang, M. J. Kramer, M. Xu, S. Wu, S. G. Hao, D. J. Sordet, K. M. Ho and C. Z. Wang, *Phys. Rev. B: Condens. Matter Mater. Phys.*, 2009, **79**, 144205.
- 48 O. N. Senkov, D. B. Miracle, E. R. Barney, A. C. Hannon, Y. Q. Cheng and E. Ma, *Phys. Rev. B: Condens. Matter Mater. Phys.*, 2010, **82**, 104206.
- 49 S. Y. Luo, J. H. Li, J. B. Liu and B. X. Liu, *Acta Mater.*, 2014, **76**, 482–492.
- 50 T. Fukunaga, K. Itoh, T. Otomo, K. Mori, A. Sugiyama, H. Kato, A. Hasegawa, A. Hirata, Y. Hirotsu and A. C. Hannon, *Mater. Trans.*, 2007, **48**, 1698–1702.
- 51 S. Q. Wu, C. Z. Wang, S. G. Hao, Z. Z. Zhu and K. M. Ho, *Appl. Phys. Lett.*, 2010, **97**, 021901.
- 52 A. Takeuchi and A. Inoue, *Mater. Trans.*, 2005, **46**, 2817–2829.